Volume 3
Number 3
7 February 2022
Pages 1307–1836

Materials Advances

rsc.li/materials-advances

ISSN 2633-5409

ROYAL SOCIETY OF CHEMISTRY

PAPER
Stephan E. Wolf *et al.*
Progressive changes in crystallographic textures of biominerals generate functionally graded ceramics

Materials Advances

ROYAL SOCIETY OF CHEMISTRY

PAPER

View Article Online
View Journal | View Issue

Cite this: *Mater. Adv.*, 2022, 3, 1527

Progressive changes in crystallographic textures of biominerals generate functionally graded ceramics†

David Wallis,‡[a] Joe Harris,‡[b] Corinna F. Böhm,[b] Di Wang,[c] Pablo Zavattieri,[c] Patrick Feldner,[d] Benoit Merle,[d] Vitaliy Pipich,[e] Katrin Hurle,[f] Simon Leupold,[g] Lars N. Hansen,[h] Frédéric Marin[i] and Stephan E. Wolf *[bi]

Received 4th November 2021,
Accepted 21st December 2021

DOI: 10.1039/d1ma01031j

rsc.li/materials-advances

Biomineralizing organisms are widely praised for their ability to generate structural materials with exceptional crystallographic control. While earlier studies highlighted near-to single-crystalline biominerals, complex polycrystalline features are more widespread yet challenging to account for. Here, we propose that biominerals whose crystal texture varies with depth are functionally graded materials. Using the exemplary case of the nacro-prismatic pearl oyster *Pinctada margaritifera*, we demonstrate systematic textural changes in a biogenic ceramic. This bivalve employs three synergistic mechanisms to generate a texture gradient across its outer calcitic shell layer. This prismatic layer transitions from an initially weakly-textured to a strongly-textured material. Such changes in texture cause a variation in Young's modulus normal to the shell, owing to the anisotropic mechanical properties of the composing crystallites. Based on finite-element simulations and indentation experiments on the bivalve shell, we conclude that such graded bioceramics yield intrinsic toughening properties similar to those found in compositionally-graded synthetic materials. Notwithstanding, the gradation concept of *Pinctada margaritifera* is unparalleled among synthetic materials as it rests solely upon elastic anisotropy, making oyster shells potential blueprints for future bioinspired functional materials and damage-resistant ceramics.

[a] *Department of Earth Sciences, University of Cambridge, Cambridge, CB2 3EQ, UK*
[b] *Department of Materials Science and Engineering, Institute of Glass and Ceramics (WW3), Friedrich-Alexander University Erlangen-Nürnberg (FAU), Martensstrasse 5, 91058 Erlangen, Germany*
[c] *Lyles School of Civil Engineering, Purdue University, West Lafayette, IN 47907-2051, Indiana, USA*
[d] *Department of Materials Science and Engineering, Institute I and Interdisciplinary Center for Nanostructured Films (IZNF), Friedrich-Alexander University Erlangen-Nürnberg (FAU), Cauerstr. 3, 91058 Erlangen, Germany*
[e] *Jülich Centre for Neutron Science JCNS, Forschungszentrum Jülich GmbH, Outstation at MLZ, Lichtenbergstr. 1, 85747 Garching, Germany*
[f] *GeoZentrum Nordbayern – Mineralogy, Friedrich-Alexander University Erlangen-Nürnberg (FAU), Schlossgarten 5a, 91054 Erlangen, Germany*
[g] *Department of Earth and Environmental Sciences, University of Minnesota, Minneapolis, 55455, USA*
[h] *UMR CNRS 6282 Biogéosciences, Université de Bourgogne Franche-Comté, 6 Boulevard Gabriel, 21000 Dijon, France*
[i] *Interdisciplinary Center for Functional Particle Systems (FPS), Friedrich-Alexander University Erlangen-Nürnberg (FAU), Haberstrasse 9a, 91058 Erlangen, Germany. E-mail: stephan.e.wolf@fau.de*

† Electronic supplementary information (ESI) available: Experimental details and supplementary figures: (S1) Macrophotograph of *Pinctada margaritifera*; (S2) Axes of 2–10° lattice rotations within Group 1, transitional, and Group 2 prisms; (S3) Stereoplots of Young's modulus for different portions of the prismatic layer; (S4) Nanoindentation analysis of compliant and stiff prisms of *P. margaritifera*; (S5) Details on the finite-element modelling; (S6) Micrographs and EBDS maps of the prismatic layer of *Pinna nobilis*; (S7) Small and very-small angle neutron scattering of powdered prisms. See DOI: 10.1039/d1ma01031j

‡ D. W. and J. H. contributed equally to this work.

I. Introduction

Biominerals are biogenic ceramic materials vital to the host organism's survival as they perform critical functions, such as in sensors,[1,2] armor,[3] or weaponry.[4,5] Millions of years of selection pressure have optimized the designs of biominerals to the extent that conserved structural motifs can serve today as inspiration for designing functional materials.[6] As structural materials, biominerals are evolutionarily optimized to attain both strength and toughness,[7] combining two material traits that are typically mutually exclusive.[8] Thus, biominerals are biologically generated ceramics that address a classic material-design challenge, how to generate hard but non-brittle materials.[9] Nature's common solution to this challenge is blending stiff and soft components in a hierarchical architecture spanning several orders of length scale.[10] This design trait of biominerals turns their mechanical response into a complex function of contributions from different length scales.[11]

Damage evolution in a ceramic material is not solely governed by its microstructure (*i.e.*, grain boundaries). It is affected by various phenomena, with toughening mechanisms ranging from crack tip interactions to crack tip shielding and crack bridging.[12] Mechanisms impacting crack initiation and propagation operate both near and in the distance to the crack tip, in its front and its wake.[13,14] In biominerals, intrinsic and

extrinsic toughening mechanisms have been identified that synergistically contribute to its overall fracture toughness.[8,15–17] Extrinsic mechanisms reduce the crack driving force and arise from microstructural elements located either behind or in the wake of the crack tip.[8,14,15,18] Crack-bridging ligaments, microcracking, and crack deflection are extrinsic mechanisms common to biominerals.[13–15,19–22] Intrinsic mechanisms work ahead of the crack tip, and they are inherent to the material and independent from discrete structural elements or interfaces.[13,14] They increase the resistance against crack initiation and growth, hindering damage mechanisms.[8,14,15,18] Uncoiling and fibrillar sliding in collagen are classic examples of intrinsic toughening mechanisms of biominerals.[8,15]

Biological materials often feature structural or compositional gradients imparting a progressive change in specific material properties.[23] For example, such gradients were found to increase contact damage resistance[4,5,23–28] or to confer interfacial strengthening and toughening.[23,29,30] Stomatopods exemplify the efficacy of this design strategy.[31] These mantis shrimps are noted for their hunting style since they employ their dactyl club as an ultrafast hammer to disrupt their preys' shells and exoskeletons. Multiple compositional gradients have been identified that provide the club with the required impact and damage tolerance.[4,5,26,28,32]

The black-lipped Polynesian pearl oyster *Pinctada margaritifera* (Pterioida order) is a prey for stomatopods;[31] it is a marine bivalve endemic to intertidal and subtidal habitats of coral reefs. The shell of *P. margaritifera* consists of an inner layer made from aragonitic nacre and an outer layer composed of calcitic columnar prisms. The oyster *P. margaritifera* is not the only specimen with a nacroprismatic shell design; a considerable number of molluscs feature a comparable shell organization.[33,34] Nacroprismatic bivalves are found in various habitats and feature subtle differences in their shell structures while exhibiting remarkable mechanical properties. For instance, the biogenic and prismatic calcite layers of the bivalves *Atrina rigida* and *Pinna nobilis* are 50–70% harder than geologic calcite.[35,36] This enhancement originates primarily from hindered dislocation motion, induced by effects such as solid-solution strengthening by Mg^{2+} incorporation[37,38] or composite strengthening by incorporated bio(macro)-molecules.[39–45] The shape of the tessellating prisms is not crystallographically controlled; it results from the shape-preserving transformation of an amorphous precursor.[43,46,47] It has been further shown that the morphogenesis of nacroprismatic shells is guided by thermodynamic constraints, such as directional solidification or grain growth,[48,49] and its crystallographic features by the mineralization kinetics.[50]

Biogenic calcite that appears to be nearly single-crystalline have attracted considerable attention.[51–53] However, only a few species generate such uniform crystalline prisms, such as *P. nobilis* or *A. rigida*, with their [*c*]-axes parallel to the growth axis of the prisms and, thus, perpendicular to the shell surface.[54–56] The calcite prisms of other species are crystallographically more complex, with various mapping experiments demonstrating their polycrystallinity. Thus, these prisms are composed of crystallographically iso-oriented subdomains (or crystallites) with distinct misorientation relative to their neighbors.[53,57–60] In the present case of *P. margaritifera*, Checa *et al.* showed that prisms initially consist of only one crystallographic subdomain, which undergoes crystal lattice tilting and eventually splits into independent subdomains.[61] These subdomains progressively align their [*a*]-axis with those of their neighbours' subdomains, a process that was explained in terms of growth competition between individual crystallites within a single prism.[62] Thus, these crystallographic features appear as a by-product of a biologically controlled crystal growth process[63,64] with distinctly fast kinetics of mineralization.[50]

A comparative study[65] on calcitic columnar prisms of seven mollusc shells suggested a biological function of crystal-lattice tilting beyond biomineral growth. It reported that calcite prisms of the two pearl oysters *Pinctada fucata* and *P. margaritifera* show the most pronounced crystal-lattice tilting and the highest hardness while also featuring the smallest crystallite sizes.[65] It concluded that tilting crystal lattices are "the structural property that confers increased hardness to the prisms of the *Pinctada* species".[65] Macroscale crystal lattice tilting is microscopically caused by a larger number of small-angle crystal boundaries.[66] Such crystallographic inhomogeneities are indeed well known to harden materials by impeding dislocation motion.[8,35,67] However, substantial hardening can also be caused *via* the Hall–Petch effect, thus by smaller grain sizes, as demonstrated in avian eggshells.[68]

In this contribution, we fathom the peculiar crystallographic layout of the prismatic calcite layer of *P. margaritifera*, through electron backscatter diffraction (EBSD). We further apply a range of complementary techniques, including indentation experiments and stress-field simulations, to assess a potential impact on mechanical properties. We demonstrate a *systematic* crystallographic texture gradient across the entire prismatic calcite layer that arises from two complementary mechanisms: (i) a cross-over in the relative proportions of prisms with different preferential orientation and (ii) crystal-lattice tilting in individual prisms. The coaction of these two mechanisms contributes to a less obvious mechanism, (iii) gradual ordering of the entire prismatic layer by a transition from an initially non- or weakly textured material to a strongly textured material. The observed crystallographic texture gradient is a product of these three well-concerted processes, an observation that led us to conjecture that the textural changes are purposeful. Since a crystal's elastic modulus depends on its orientation, the texture gradient causes a gradual change in elastic properties that transforms the prismatic shell layer into a functionally graded material. Finite-element models predict that a gradient in Young's modulus improves the material's damage resistance by imparting significant stress delocalization. Indentation experiments on the prismatic layer of *P. margaritifera* indeed show that these elastically graded prisms are optimized for wear and contact damage and demonstrate a remarkable increase in fracture toughness, compared to elastically homogenous prisms of *P. nobilis.* Based on these observations, we conclude that biominerals with crystallographic texture gradients can be seen as functionally graded materials. If suitably

oriented and of sufficient magnitude, their elastic gradation can impart stress delocalization, leading to a distinct enhancement of a bioceramic's fracture toughness and opening new bioinspired avenues to damage-resistant ceramics.

II. Results

We employed a range of methods to investigate the outer calcitic layer of the bivalve shell *Pinctada margaritifera* (Fig. S1, ESI†), which consists only of calcite columns separated by a periprismatic organic matrix (Fig. 1a and b). Prisms are composed of crystallites, which form crystallographic subdomains if their mutual misorientation is small.[61] As shell growth proceeds from the exterior to the interior by layer-by-layer deposition, the shell records a time series progressing from the outside to the inside of the shell (top to bottom in Fig. 1a and c–f).[63]

II.1. Electron backscatter diffraction (EBSD) analyses reveal crystallographic texture gradients

Electron backscatter diffraction (EBSD) maps of the outer calcitic layer show systematic crystallographic texture gradients across its entire thickness, which arise from independent crystallographic changes across length scales, from the crystallite level up to the level of the entire prismatic layer.

The EBSD map presented in Fig. 1c covers the complete cross-section of the prismatic layer between the exterior (top) and interior (bottom) boundaries. The crystallographic orientations of the prisms define two end-member groups, with some prisms being transitional between these end-members (Fig. 1d–f). Many prisms near the shell's exterior, Group 1, have [*c*]-axes typically at less than $\sim 50^\circ$ to the growth direction (Fig. 1d). However, the largest area fraction consists of prisms, Group 2, with [*c*]-axes lying approximately within the plane of the shell (Fig. 1e). Our classification is in line with recent studies reporting on an unexpected growth direction of late prisms in *P. margaritifera* perpendicular to the [*c*]-axis, *i.e.*, of Group 2 prisms in our terminology.[69]

A smaller set of prisms, termed 'transitional', have [*c*]-axes that start in similar orientations to those of Group 1. However, during progressive growth, the [*c*]-axes of their intraprismatic crystallites rotate by up to 68° to lie approximately within the plane of the shell (Fig. 1f); they represent a transmutation of Group 1 prisms into Group 2 prisms. All prisms contain significant orientation gradients, with [*c*]-axis orientations typically varying by several tens of degrees within a single prism, as illustrated in detail in Fig. 2. This phenomenon of crystal-lattice tilting has been first described by Checa and co-workers.[61]

In all groups, the misorientation axes of domain boundaries with misorientation angles in the range $2–10^\circ$ are parallel to either an $\langle a \rangle$-axis or $\{m\}$-pole, *i.e.*, $\{11\bar{2}0\}$ or $\{10\bar{1}0\}$ However, these misorientation axes have different spatial orientations in each group of prisms (due to their different crystal orientations), leading to differing evolution of lattice orientation during prism growth (Fig. S2, ESI†). The axes of lattice rotation in Group-1 prisms are typically oblique to both the plane of the shell and to the growth direction (Fig. 2a and Fig. S2, ESI†). Thus, the crystal-lattice tilting in Group 1 prisms rotates the [*c*]-axis towards the plane of the shell during progressive growth, but their growth terminates before their [*c*]-axes reach the plane of the shell. In Group 2 prisms, out of the three symmetrical equivalents of both $\{m\}$-poles and/or $\langle a \rangle$-axes, rotation commonly occurs around the variant parallel to the growth direction (Fig. 2b). This constrains the [*c*]-axes of Group 2 prisms to remain within the plane of the shell during growth. In transitional prisms, the [*c*]-axes become aligned parallel to the plane of the shell and remain so during extensive further growth (Fig. 2c). Consequently, in all groups, [*c*]-axes either rotate toward and/or remain within the plane of the shell during progressive growth.

Overall, we observe a texture gradient due to two apparent mechanisms: (i) changes in the relative proportions of prisms from Groups 1 and 2; and (ii) crystal-lattice tilting, *i.e.*, systematic crystallite-to-crystallite rotations (thus of subdomains within prisms), progressively aligning the $\langle a \rangle$ and $\{m\}$ directions with the growth direction and the [*c*]-direction with the plane of the shell.

The first mechanism can be easily explained by Grigor'ev crystal-growth competition on the prism level, in which crystals with their fastest growth axis oriented approximately perpendicular to the substrate outcompete others and dominate the late stage of prism growth.[70] The crystallographic orientation of the prisms and their geometrical evolution indeed indicate that prism growth rates are crystallographically controlled and that $\langle a \rangle$ and/or $\{m\}$ are the fastest growth directions in this mineralization system. For calcite, growth along the [*c*]-axis is commonly fastest during growth from solution. However, under diffusion-limited conditions, such as by the action of face-specific growth inhibitors or under spherulitic and pseudomorphic growth conditions, other growth directions may take over.[66]

The second mechanism, crystal lattice tilting, is well-documented in synthetic crystalline materials, such as calcite films generated *via* a nonclassical biomimetic crystallization route.[66,71] In such materials, occluded impurities trigger largely uncontrolled autodeformation and non-crystallographic branching. Specialized intracrystalline biomineralization proteins possibly trigger the misorientations in *P. margaritifera* by comparable, but precisely controlled, mechanisms, as suggested by Checa and co-workers.[53,61]

The coaction of these two mechanisms enable a third mechanism: (iii) gradual crystallographic ordering. The combination of mechanisms (i) and (ii) yields both a textural gradient and an increasing texture strength. Prisms of Group 2 (Fig. 1f) have a stronger texture (evident as tighter clusters in the pole figures) than prisms of Group 1 (Fig. 1d). This effect can be quantified using the J-index,[72] which provides a measure of texture strength. Group 1 has a J-index of 5.5, whereas Group 2 has a J-index of 8.9. This contrast in texture strength records a progressive disorder-to-order transition across the shell thickness.

II.2. Crystallographic gradients modulate mechanical properties

The texture gradients inevitably change the directional mechanical properties of the entire prismatic layer as the constitutive

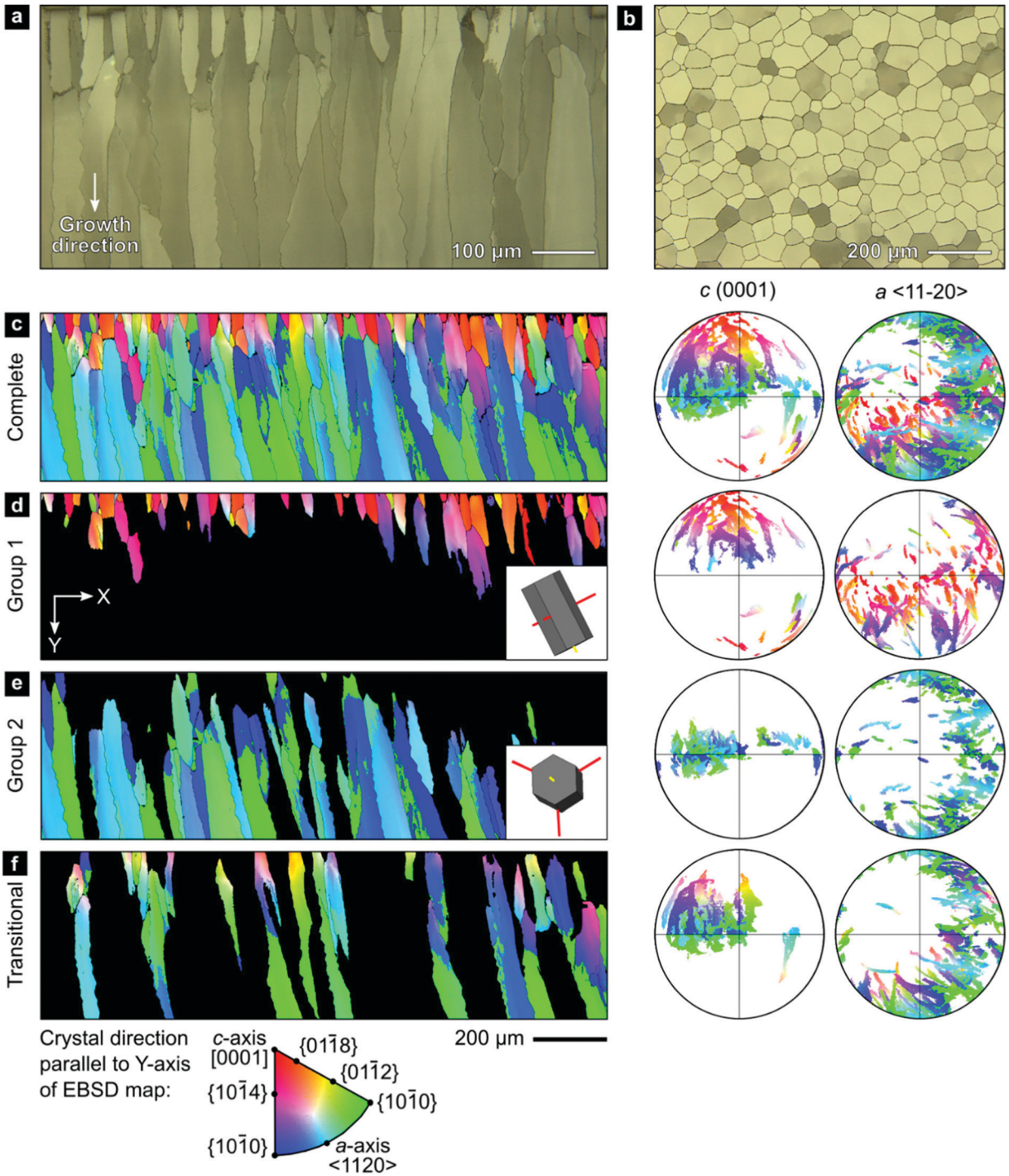

Fig. 1 Crystallographic orientations in the prismatic layer of *Pinctada margaritifera*. (a and b) Polarized reflected light micrographs of sections of the prismatic layer perpendicular and parallel to the shell surface. (c–f) EBSD maps and corresponding pole figures for the complete dataset and subsets of Group-1 prisms, Group-2 prisms, and transitional prisms. All maps and pole figures are in the same reference frame and are colored according to the inverse-pole-figure legend indicating the crystallographic direction aligned with the *Y*-direction of the map, *i.e.*, perpendicular to the shell surface. The inset images in subfigure d and e indicate typical crystal orientations within each group.

crystallites have anisotropic mechanical properties. We demonstrate this effect using the directionality of Young's modulus in calcite, illustrated in Fig. 3a, as the anisotropic elastic properties of constituent crystallites control the effective stiffness of the prismatic layer. We employed effective-medium theory based on crystal orientation distributions and the anisotropic elastic stiffness tensor for calcite to estimate Young's modulus perpendicular to the shell surface.[73,74] Mechanical properties in this direction are of particular interest as this is a likely direction of impacts to the shell.

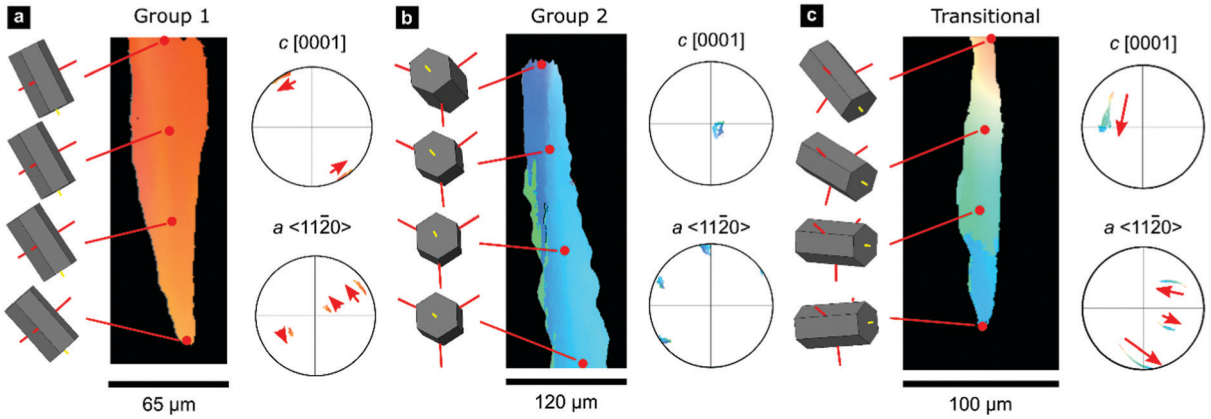

Fig. 2 Gradients in crystallographic orientation within calcite prisms of *P. margaritifera*. Maps and pole figures of Group-1, Group-2, and transitional prisms colored according to the inverse pole figure for the *Y*-direction, inset in Fig. 1c.

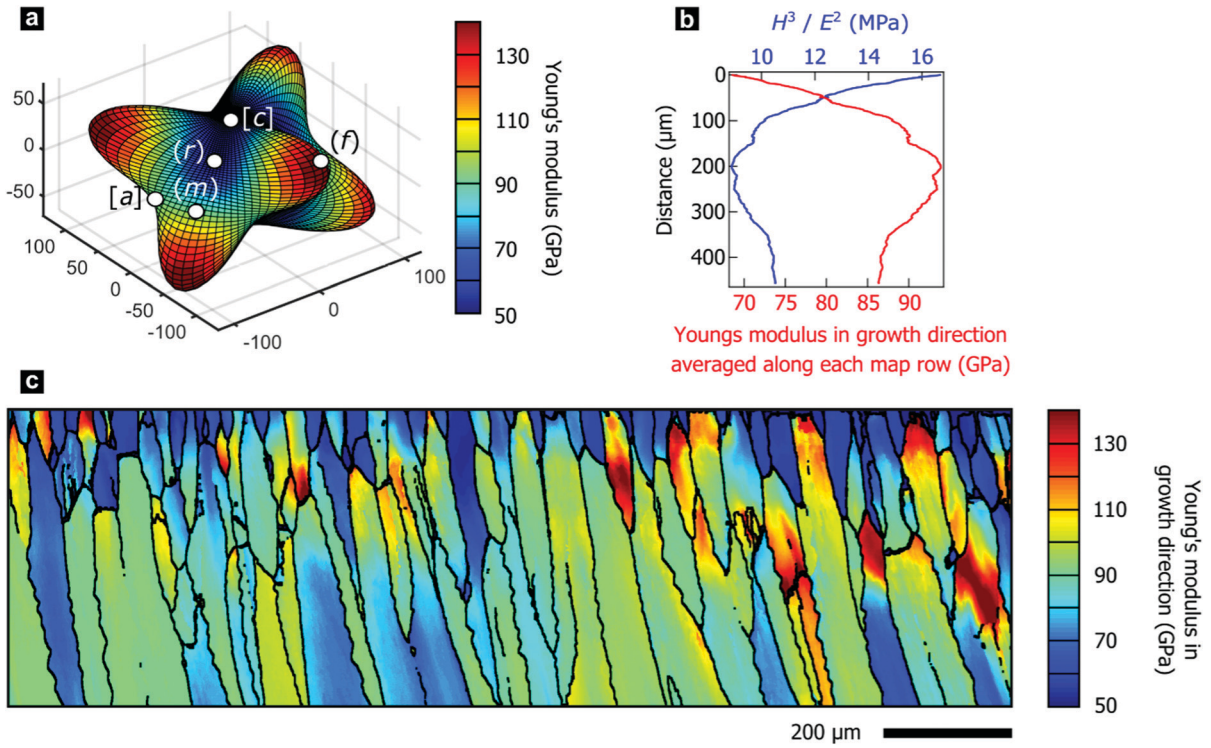

Fig. 3 (a) Three-dimensional visualization of the anisotropic Young's modulus in a calcite single crystal. (b) Young's modulus in *Y*-direction averaged per line and H^3/E^2, a measure of wear resistance, as a function of distance from the shell exterior. (c) Calculated Young's modulus in the *Y*-direction of the map, *i.e.*, perpendicular to the shell's surface and, thus, parallel to the growth direction.

In *P. margaritifera*, the Young's modulus exhibits systematic gradients across the mapped area, both within individual prisms (Fig. 3c), and across the overall microstructure (Fig. 3b). Fig. 3b demonstrates that, in general, the Young's modulus normal to the shell surface increases with progressive growth. The initially low and heterogeneous Young's modulus is gradually transformed into a high and homogeneous Young's modulus during the first ~0 µm of growth of the prismatic layer (Fig. 3b and c and Fig. S3, ESI†).

The variable elastic properties necessarily alter the macroscale mechanical performance of the prismatic layer, which is crucial for the mechanical resistance of the protective shell. We performed nano-indentation parallel to the growth direction at a range of depth positions within the prismatic layer, which revealed the hardness to be approximately constant at 4.28 ± 0.35 GPa. This value agrees well with the literature and is comparable to other nacroprismatic bivalves such as *P. nobilis*.[36,75] As wear resistance scales with the relation H^m/E^n ($m \geq n \geq 1$), where H denotes the hardness and E the elastic modulus,[76] wear resistance of the prismatic layer is highest at the exterior where the material is most compliant (Fig. 3b). Furthermore, we experimentally characterized intraprismatic

crack initiation by nano-indentation, which probes length scales up to a few micrometers.[77–79] Displacement bursts in the continuous load–displacement curves coincided with the appearance of visible cracks and therefore resulted from crack initiation (Fig. S4, ESI†). The probability distributions of crack initiation as a function of the indentation force demonstrate that the compliant prisms of Group 1, which dominate the shell exterior, consistently require greater indenter loads to initiate fracture than the stiffer prisms of Group 2 (Fig. S4e, ESI†). This shows that the mechanical properties of the prismatic layer of *P. margaritifera* are optimized for resistance to wear and surface damage.

II.3. Elastic gradients modulate a material's stress field

The progressively changing crystal texture, which imparts a change in stiffness normal to the shell surface, may thus transform the prismatic layer into a functionally graded material. Theoretical studies found that elastic gradients can confer distinct flaw-tolerance through their impact on stress distribution, albeit this effect is sensitive to other material characteristics, such as the Poisson's ratio.[80–82] Only an elastic gradient that shows a suitable orientation and a sufficient elastic variation can reduce the stress at a crack tip and therefore intrinsically toughen a given material. Experimentally, Suresh and co-workers have impressively evidenced improved contact-damage tolerance for the case of compositionally-graded silicon nitrides.[83–85] Such results could imply an additional biological function of graded textures in biominerals: crystallographic gradients may serve as a toughening motif increasing the contact-damage tolerance of mineralized armatures. However, this raises the question of whether the observed change in the elastic modulus is already sufficient and suitable to allow for similar toughening mechanisms.

To address this question, we employed finite-element modelling simulations. In these simulations, we studied a surface crack under a tensile load by subjecting a notched strip of material to a pure remote mode I loading. We compared a reference model characterized by a homogenous Young's modulus with models that feature graded, inverse graded, or discrete multi-layered Young's moduli in vertical direction under identical loading conditions (Fig. S5, ESI†). The purpose of these simulations is to provide insights into the role of gradients on the local stress intensity factor. We surmise that resistance to crack propagation provides a local hardening mechanism that contributes to the delocalization of microcracks, and thus, contributing to the overall toughness of the material. We hypothesize that the effect of grain orientation and anisotropy has a lesser effect, where the resistance to crack propagation is mainly driven by the gradient in the stiffness. For each case, the fracture resistance was quantified in terms of the predicted stress-intensity factor (K_I) as a function of crack length, plotted in Fig. 4a and b. In these simulations, the graded model outperforms all control materials by exhibiting the lowest stress intensity factor. The graded model experiences stress-intensity factors up to 20% lower than the homogenous material, and thus such a structure would lead to a notable improvement in fracture resistance. By distributing the stress widely across the bulk, the gradient improves the damage tolerance as it diminishes the stress intensity at the crack tip, as illustrated in Fig. 4c. In contrast and as a control, the opposite is true when the gradient is reversed. These simulations show that the observed elastic gradient is already sufficient to have a notable effect on the fracture toughness of a given material.

We undertook indentation experiments to validate these theoretical predictions. Based on these simulations, one would predict that the graded prismatic layer found in *P. margaritifera* features improved damage resistance compared to a non-graded counterpart. Such a non-graded control is essentially given by the prismatic calcite layer of *P. nobilis*: it is composed of co-oriented crystallites with [*c*]-axes normal to the plane of the shell, thus, with a crystallographic orientation similar to Group-1 prisms of *P. margaritifera*, see Fig. S6 (ESI†).[46,86] We undertook indentation experiments, in which we compare *P. margaritifera* to *P. nobilis*, which can be seen as an elastically homogenous counterpart, along with geological calcite as a reference. Crack formation caused by the employed indentation experiments has been shown to occur under mode I loading, making these experiments comparable to our simulations.[87,88] To probe the impact of the observed elastic gradient on the fracture toughness, we conducted Vickers microhardness tests. In the case of brittle solids, these tests probe depth ranges of approximately 75–100 μm, the scale over which Young's modulus of the oyster shell varies on the order of 25%. Vickers indentation under identical loading conditions resulted in an extended fracture, shattering, and disaggregation of both geological calcite and *P. nobilis* prisms in and around the indents, illustrated in Fig. 4d. In stark contrast, *P. margaritifera* endured the indentation with only minimal fracture. The Vickers tests further allowed for quantification of the materials' fracture toughness. Geological calcite exhibited a fracture toughness of 0.34 ± 0.04 MPa m^{-1}, whereas *P. nobilis* demonstrated a distinctly increased fracture toughness of 1.16 ± 0.49 MPa m^{-1}, which we attribute to its hierarchical organization (see below). The crystallographically graded prismatic layer of *P. margaritifera* surpasses even *P. nobilis*, with a superior fracture toughness of 3.15 ± 1.86 MPa m^{-1}. The superior mechanical performance of the prismatic layer of *P. margaritifera* demonstrates an optimized damage resistance.

Hardening and toughening may also arise by other, potentially unidentified structural features, such as changes in the hierarchical and ultrastructural organization or changes in the crystallite size, as discussed in the introduction. The typical size of prism of *P. nobilis* (Fig. S6 and Fig. 4d) appears to be larger than that Group I prisms of *P. margaritifera* (Fig. 2 and 4d) whereas Group 2 and transitional prisms (Fig. 1 and 2) are comparable in diameter. Our modelling does not capture this gradual increase in prism diameter, as the analysis of crack path deviation caused by the periprismatic sheaths are beyond the scope of this study. To assure that prisms of both species feature a similar internal ultrastructural organization and are thus indeed comparable, we employed both small-angle neutron scattering and anisotropic Scherrer analyses. Both, *P. margaritifera* and *P. nobilis* have been repeatedly reported to feature a similar ultrastructure with nanograins a few tens of

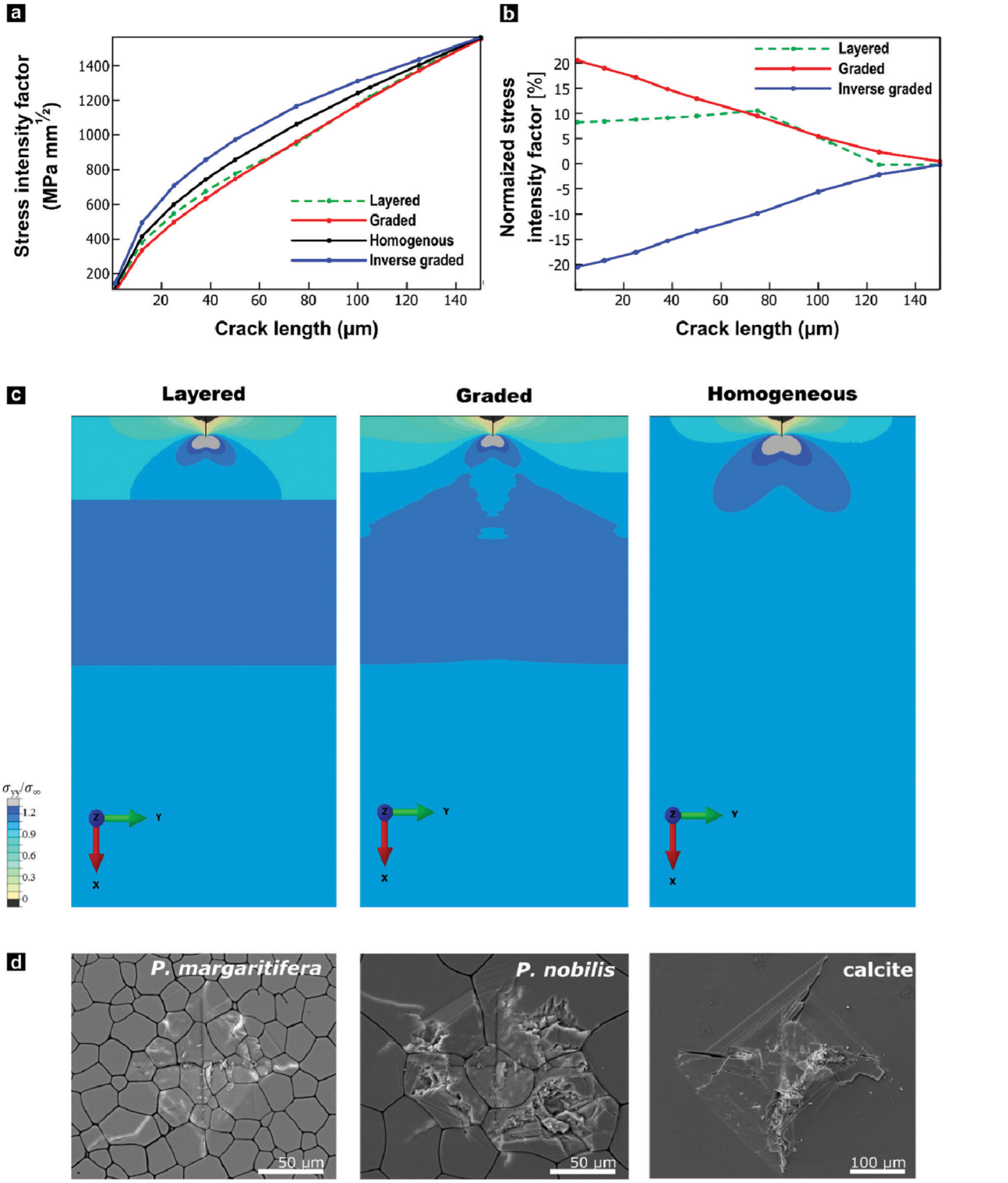

Fig. 4 Mechanical impacts of the functional gradient in *P. margaritifera* predicted by finite-element modelling and tested by Vickers microindentation. (a) Stress-intensity factor at the crack tip as a function of crack length. (b) Stress-intensity factor of graded, inverse graded, and layered materials normalized with respect to the homogeneous material, as a function of crack length. (c) Spatial distributions of the σ_{yy} component of stress normalized by the applied boundary stress (σ_∞) around a 25 μm crack. (d) Optical micrographs of comparative Vickers microhardness tests on *P. margaritifera*, *P. nobilis*, and geological calcite.

nanometres in size,[41,46,61,86,89] which similarly have been found in other calcareous biominerals, such as nacre.[63,90–92] We probed the sub-prismatic crystallite morphology by anisotropic Scherrer analyses,[93] which provided spatial dimensions of the coherently scattering domains. In the case of geological calcite, the crystallite sizes were beyond the range of this approach

(>1000 nm), which demonstrates that this control calcite was well-crystalline. In contrast, we found that the crystallite morphologies in prisms of both bivalves feature a notable and comparable asymmetric layout. Their coherently scattering domains largely stretch out in the (*hk*0) directions (>1000 nm), but they are confined to some few hundreds of nanometres in the (001) direction. Thus, the crystalline domains of *P. nobilis* and *P. margaritifera* prisms have both a prolate shape with comparable aspect ratios and lateral dimensions of 200 ± 50 nm and 450 ± 200 nm, respectively. It should be noted that recent ptychography studies demonstrated that crystalline coherence also expand across a couple of granules.[53]

Small-angle neutron scattering (SANS) in the small- and very-small angle regime confirmed that the hierarchical organization of prisms extracted from both species is comparable, especially on the sub-micron length scale. Both types of calcite prisms are fractal materials characterized by a Porod exponent of 3, which suggests a three-dimensional network of particles.[94] This inference is consistent with the observation that bivalve shell growth can proceed *via* the aggregation of nanosized particles.[63,95] A multi-level Beaucage fit reveals further structural elements across scales; thus, a hierarchical order of building units, see Fig. S7 (ESI†).[96] The powdered calcite prisms of *P. nobilis* are composed of three different units with diameters of approximately 0.55 μm, 45 nm, and 1.4 nm, respectively. In *P. margaritifera*, again, three structural units are found, with similar characteristic gyration radii of 0.87 μm, 40.8 nm, and 2.2 nm. We assume that the structural units with a diameter of 0.55 and 0.87 μm reflect the particle sizes of the powdered samples as no larger units are detected. The following structural elements with an approximate diameter of about 40 nm fit well with the reported size of the mineral nanogranules,[41,46,61,86,89] whose self-assembly probably drives shell formation in these bivalves.[63,95] The smallest component identified by SANS is in the low nanometre range. Their diameter is consistent with reports on the intergranular organic matrix, which can be described as a holey organic envelope of the nanogranules or an extended interstitial network with a 1–2 nm thickness.[40,46,61,97] We also determined the mass fraction of this intracrystalline organic matrix by thermogravimetric analysis (TGA) and found a similar amount of about 0.5–1% in both species. The results obtained from two different scattering methods and TGA validate our assumption that the prismatic layer of *P. nobilis* represents a comparable but non-graded counterpart to the crystallographically graded prismatic layer of *P. margaritifera*.

III. Discussion and conclusions

Our results demonstrate that, concealed by the crystallographic complexity of its shell, the black-lipped pearl oyster employs three mechanisms to systematically generate a crystallographic texture gradient across its entire prismatic calcite layer. We identified two evident and complementary mechanisms that act on different length scales: (i) crystal-lattice tilting within prisms and (ii) a ratio cross-over of prisms with different preferred crystal orientations. The synergistic cooperation of these two phenomena gives rise to a rather concealed third mechanism: (iii) gradual ordering, *i.e.*, a disorder-to-order transition from weak to strong texture. The gradual change in crystallographic texture is inevitably accompanied by a gradual change in directional elastic properties since the constituting crystallites are elastically anisotropic. We tested by finite-element modelling whether the elastic gradient observed in *P. margaritifera* would be suitably oriented and sufficient in magnitude to impart stress delocalization, as reported in the case of compositionally-graded synthetic ceramics. These simulations confirm that the observed gradients are suitable and can provide considerable intrinsic toughening.

By employing nano-indentation and Vickers indentation, we validated that the mechanical performance of *P. margaritifera* is indeed commensurate with the expected mechanical behaviour of an elastically-graded material. Nano-indentation experiments showed that the prismatic layer is optimized concerning wear resistance, as it exposes its most compliant surface to the environment. This directional layout provides another beneficial effect; greater loads are needed to initiate fracture, further optimizing the shell's resistance against sharp contact damage. Based on the finite-element simulations, one would expect that an elastically graded prismatic layer features an increased fracture toughness compared to a non-graded, homogenous prismatic layer. Vickers indentation, which probes depth ranges commensurate with the dimensions of the observed gradient, found that the prismatic layer of *P. margaritifera* features a fracture toughness of 3.15 ± 1.86 MPa m^{-1}. This value surpasses the fracture toughness of the elastically-homogenous prismatic layer of *P. nobilis* (1.16 ± 0.49 MPa m^{-1}). However, this value cannot be quantitatively compared with our finite element predictions, which captures only the local toughening due to the elastic gradient. Such localized intrinsic toughening enables additional extrinsic mechanisms (*i.e.*, microcracking), which promote the spread of damage to a greater volume, thereby increasing energy dissipation and toughness. Then, a collective behaviour of delocalization effects leads to the experimentally measured values exceeding those determined in our simulations. The spread of damage in the outer calcite layer of *P. margaritifera* supports our hypothesis that delocalization effects contribute to its toughness (Fig. 4d). Its behaviour in indentation experiments clearly deviates from the expected and observed brittle behaviour of geological calcite (Fig. 4d), which has a fracture toughness an order of magnitude lower than the calcitic prismatic layer of *P. margaritifera*. In the case of brittle calcite, damages highly localizes into major cracks that ultimately lead to catastrophic brittle failure—as expected for a brittle mineral. In stark contrast, biological materials typically exhibit widespread damage and flaw tolerance. Biological materials owe this distinctive trait to the presence of weak crack initiation sites (*e.g.*, imperfections) that stimulate the nucleation and growth of additional and secondary cracks. In coaction with clever crack arrest mechanisms, these mechanisms give rise to delocalization, spread of damage and, as consequence, to enhanced energy absorption which contributes to the toughness.[98] Our finite element simulations provide insights on how an elastic gradient can contribute to these local

toughening mechanisms promoting crack arrest. Ultimately, the overall toughness of a material—as the one measured in our nanoindentation experiments—has to be seen as a representation of the collective behaviour of all microcracks. This explains the effect of delocalization and spread of damage on the fracture toughness of *P. margaritifera*.

Recent studies on nacre showed that nanogranular biominerals exhibit coherent and continuous stress contours in their mesoscale building units across nacre tablets.[99] Nano-indentation experiments on nacre, followed *in situ* by high-resolution transmission electron microscopy, revealed those microstructural elements to interlock when loaded. Thus, strain contours can propagate across the microstructural elements in a relatively unhindered manner.[90] Both experimental studies exemplified that mesoscale units cooperatively act when spreading the stress field,[90,99] which allowed us to focus our simulations on the wider stress field by employing simplified structural models.

To exclude that the observed increase in fracture toughness results from unidentified structural differences between the two species, such as distinct changes in crystallite sizes, we performed small- to very-small angle neutron scattering and anisotropic Scherrer analyses. By thermogravimetric analyses (TGA), we also precluded that the observed mechanical differences originate in compositional differences, *e.g.*, varying fractions of intracrystalline organics. With two different scattering methods in concert with TGA analyses, the prisms of *P. nobilis* turn out as suitable homogenous equivalents to the crystallographically-graded prisms of *P. margaritifera*.

Building on our cross-scale characterization of the prismatic layer of the oyster shell *P. margaritifera* summarized above and guided by the results of our finite-element simulations, we suggest that biominerals with crystallographic texture gradients are elastically-graded materials that feature distinctly modulated stress fields and stress intensity factors. These conclusions also imply that not only species with unidirectionally and near-single-crystalline bioarmor employ crystallographic control to optimize function.[56] The functionally beneficial change of crystallite orientation during growth generates materials with complex and ostensibly unsystematic texture that stand out with excellent and complex mechanical properties. Such elastic gradients are potentially widespread in protective biomaterials, and we expect that other design principles, such as amorphous-to-crystalline or compositional changes, will also confer increased damage resistance. It should be stressed that the orientation of the elastic gradient determines the stress-field modulation, as shown by our simulation of an inverse elastic gradient.

We thus conclude that a functional gradient optimizes the molluscan body armour of *P. margaritifera*, which toughens the shell against catastrophic failure by spreading the stress field into the bulk, increasing its fracture toughness, and simultaneously optimizing the shell's resistance against wear and crack initiation at its exterior. In selected cross-lamellar shells, such as *Charonia lampas lampas* and *Cypraea testudinaria*, transverse texture gradients have been reported while near-to-no elastic gradients are present orthogonal to the shell surface.[100,101] Such transverse gradients will have a notably different impact on the biomechanics of the shell, probably affecting its resistance against shear loading rather than impact damage.[100,101] We thus anticipate that a wealth of seemingly poorly ordered biogenic materials (*e.g.*, in Unionidae[49,102]) or bioceramics with changing textures (*e.g.*, crustacean cuticles[100] or even bone[16,17,103]) use comparable concepts to (additionally) generate elastic gradients. Therefore, complex but changing crystallographic textures of biominerals should be perceived as a functionally optimized motif rather than a mere non-functional outcome of an intricate biological control over crystal growth.

Using the example of *P. margaritifera*, we further suggest a novel design principle for the toughening of (bio-)ceramics based on graded textures. We demonstrated that a gradient in average crystallographic orientations, *i.e.*, in crystallographic texture, can be an efficient way to modulate the mechanical properties of a (biogenic) ceramic. Synthetic materials or ceramics have not yet exploited the directionality of elastic properties in crystalline material and, thus, the black-lipped pearl oyster represents a blueprint for future bioinspired functional materials. This elegant concept applies to a wide range of material classes with anisotropic elasticity, heralding new design approaches towards architectured materials and novel non-brittle but tough ceramics.

Future work will focus on simulating large volumes to validate our hypothesis that the observed hardening results from local toughening stress delocalization. This mechanism, which is not captured in our simulations, involves the formation and growth of secondary microcracks, leading to increased energy dissipation and damage spreading.

Author contributions

D. W. conducted EBSD measurements, L. N. H. and D. W. analyzed the EBSD data; D. W., J. H., and S. E. W. interpreted the EBSD data; V. P. and S. E. W. analyzed and interpreted the SANS data; D. W. and P. Z. designed and conducted the F. E. M. modelling; C. F. B., J. H., P. F. conducted nano-indentation experiments under supervision of BM and analyzed the results; J. H., C. F. B., and S. L. conducted further characterization of the bivalve specimens; K. H. conducted anisotropic Scherrer analyses; F. M. provided specimens and biological context and contributed to the interpretation of the results; S. E. W. conceived the study. With the input of all other authors, D. W., J. H., and S. E. W. wrote the manuscript.

Conflicts of interest

There are no conflicts to declare.

Acknowledgements

SEW acknowledges financial support by an Emmy Noether starting grant by the Deutsche Forschungsgemeinschaft (DFG, German Research Foundation), grant number 251939425. SEW and SL received further support by the Bavarian State Ministry

of the Environment and Consumer Protection in the framework of the project network *BayBionik*, a collaborative research group (sub-project TUT01UT-73842, Grant holder SEW). DW and LNH acknowledge support from the Natural Environment Research Council Grant NE/M000966/1. DW and PZ acknowledge financial support from the Multi-University Research Initiative (AFOSR-FA9550-15-1-0009). BM and PF acknowledge financial support from DFG *via* the research training school GRK1896: ''*In Situ* Microscopy with Electrons, X-rays and Scanning Probes'' and the 'Center for Nanoanalysis and Electron Microscopy' (CENEM) at FAU. We thank J. Reiser and Dr J. Kaschta, and the Institute of Polymer Materials (LSP) at FAU for their support in TGA measurements.

Notes and references

1 B. A. Palmer, G. J. Taylor, V. Brumfeld, D. Gur, M. Shemesh, N. Elad, A. Osherov, D. Oron, S. Weiner and L. Addadi, *Science*, 2017, **358**, 1172–1175.
2 J. Aizenberg, S. Weiner, A. Tkachenko, L. Addadi and G. Hendler, *Nature*, 2001, **412**, 819–822.
3 L. Li and C. Ortiz, *Nat. Mater.*, 2014, **13**, 501–507.
4 J. C. Weaver, G. W. Milliron, A. Miserez, K. Evans-Lutterodt, S. Herrera, I. Gallana, W. J. Mershon, B. Swanson, P. Zavattieri, E. DiMasi and D. Kisailus, *Science*, 2012, **336**, 1275–1280.
5 S. Amini, M. Tadayon, S. Idapalapati and A. Miserez, *Nat. Mater.*, 2015, **14**, 943–950.
6 M. E. Csete and J. C. Doyle, *Science*, 2002, **295**, 1664–1669.
7 S. E. Naleway, J. R. A. Taylor, M. M. Porter, M. A. Meyers and J. McKittrick, *Mater. Sci. Eng., C*, 2016, **59**, 1143–1167.
8 U. G. K. Wegst, H. Bai, E. Saiz, A. P. Tomsia and R. O. Ritchie, *Nat. Mater.*, 2014, **14**, 23–36.
9 S. E. Naleway, M. M. Porter, J. McKittrick and M. A. Meyers, *Adv. Mater.*, 2015, **27**, 5455–5476.
10 M. A. Meyers, P.-Y. Chen, A. Y.-M. Lin and Y. Seki, *Prog. Mater. Sci.*, 2008, **53**, 1–206.
11 O. B. A. Agbaje, R. Wirth, L. F. G. Morales, K. Shirai, M. Kosnik, T. Watanabe and D. E. Jacob, *R. Soc. Open Sci.*, 2017, **4**, 170622.
12 D. J. Green, *An introduction to the mechanical properties of ceramics*, Cambridge University Press, Cambridge, UK, 1998.
13 T. Oh, J. Rödel, R. Cannon and R. Ritchie, *Acta Metall.*, 1988, **36**, 2083–2093.
14 R. O. Ritchie, *Nat. Mater.*, 2011, **10**, 817–822.
15 M. E. Launey, M. J. Buehler and R. O. Ritchie, *Annu. Rev. Mater. Res.*, 2010, **40**, 25–53.
16 T. A. Grünewald, M. Liebi, N. K. Wittig, A. Johannes, T. Sikjaer, L. Rejnmark, Z. Gao, M. Rosenthal, M. Guizar-Sicairos, H. Birkedal and M. Burghammer, *Sci. Adv.*, 2020, **6**, eaba4171.
17 I. Silva Barreto, S. Le Cann, S. Ahmed, V. Sotiriou, M. J. Turunen, U. Johansson, A. Rodriguez-Fernandez, T. A. Grünewald, M. Liebi, N. C. Nowlan and H. Isaksson, *Adv. Sci.*, 2020, **7**, 2002524.
18 R. O. Ritchie, *Philos. Trans. R. Soc., A*, 2021, **379**, 20200437.
19 B. Kahler, M. V. Swain and A. Moule, *J. Biomech.*, 2003, **36**, 229–237.
20 S. Kamat, X. Su, R. Ballarini and A. H. Heuer, *Nature*, 2000, **405**, 1036–1040.
21 F. Eltit, V. Ebacher and R. Wang, *J. Struct. Biol.*, 2013, **183**, 141–148.
22 D. Vashishth, K. Tanner and W. Bonfield, *J. Biomech.*, 2000, **33**, 1169–1174.
23 Z. Liu, M. A. Meyers, Z. Zhang and R. O. Ritchie, *Prog. Mater. Sci.*, 2017, **88**, 467–498.
24 B. J. F. Bruet, J. Song, M. C. Boyce and C. Ortiz, *Nat. Mater.*, 2008, **7**, 748–756.
25 Y. Politi, M. Priewasser, E. Pippel, P. Zaslansky, J. Hartmann, S. Siegel, C. Li, F. G. Barth and P. Fratzl, *Adv. Funct. Mater.*, 2012, **22**, 2519–2528.
26 S. Amini, A. Masic, L. Bertinetti, J. S. Teguh, J. S. Herrin, X. Zhu, H. Su and A. Miserez, *Nat. Commun.*, 2014, **5**, 3187.
27 B. Bar-On, F. G. Barth, P. Fratzl and Y. Politi, *Nat. Commun.*, 2014, **5**, 3894.
28 N. Guarín-Zapata, J. Gomez, N. Yaraghi, D. Kisailus and P. D. Zavattieri, *Acta Biomater.*, 2015, **23**, 11–20.
29 V. Imbeni, J. J. Kruzic, G. W. Marshall, S. J. Marshall and R. O. Ritchie, *Nat. Mater.*, 2005, **4**, 229–232.
30 S. Bechtle, T. Fett, G. Rizzi, S. Habelitz, A. Klocke and G. A. Schneider, *Biomaterials*, 2010, **31**, 4238–4247.
31 J. H. Pit and P. C. Southgate, *Aquacult. Int.*, 2003, **11**, 545–555.
32 Y. Zhang, O. Paris, N. J. Terrill and H. S. Gupta, *Sci. Rep.*, 2016, **6**, 26249.
33 O. B. A. Agbaje, I. Ben Shir, D. B. Zax, A. Schmidt and D. E. Jacob, *Acta Biomater.*, 2018, **80**, 176–187.
34 O. B. Bøggild, *The shell structure of the mollusks*, A.F. Høst & søn, København, 1930.
35 M. E. Kunitake, L. M. Mangano, J. M. Peloquin, S. P. Baker and L. A. Estroff, *Acta Biomater.*, 2013, **9**, 5353–5359.
36 C. F. Böhm, P. Feldner and B. Merle, *Materials*, 2019, **12**, 1–9.
37 B. Pokroy, A. N. Fitch, F. F. Marin, M. Kapon, N. Adir and E. Zolotoyabko, *J. Struct. Biol.*, 2006, **155**, 96–103.
38 M. E. Kunitake, S. P. Baker and L. A. Estroff, *MRS Commun.*, 2012, **2**, 113–116.
39 J. Aizenberg, J. Hanson, T. F. Koetzle, S. Weiner and L. Addadi, *J. Am. Chem. Soc.*, 1997, **119**, 881–886.
40 H. Li, H. L. Xin, M. E. Kunitake, E. C. Keene, D. A. Muller, L. A. Estroff and A. Muller, *Adv. Funct. Mater.*, 2011, **21**, 2028–2034.
41 Y. Dauphin, *Mineral. Mag.*, 2008, **72**, 243–246.
42 B.-A. Gotliv, N. Kessler, J. L. Sumerel, D. E. Morse, N. Tuross, L. Addadi and S. Weiner, *ChemBioChem*, 2005, **6**, 304–314.
43 F. Nudelman, H. H. Chen, H. A. Goldberg, S. Weiner and L. Addadi, *Faraday Discuss.*, 2007, **136**, 9–25.
44 F. Marin, B. Pokroy, G. Luquet, P. Layrolle and K. De Groot, *Biomaterials*, 2007, **28**, 2368–2377.
45 Y. Dauphin, J. P. Cuif, J. Doucet, M. Salomé, J. Susini and C. T. Willams, *J. Struct. Biol.*, 2003, **142**, 272–280.

46 S. E. Wolf, I. Lieberwirth, F. Natalio, J.-F. Bardeau, N. Delorme, F. Emmerling, R. Barrea, M. Kappl and F. Marin, *Faraday Discuss.*, 2012, **159**, 433.
47 S. Weiner and L. Addadi, *Annu. Rev. Mater. Res.*, 2011, **41**, 21–40.
48 B. Bayerlein, P. Zaslansky, Y. Dauphin, A. Rack, P. Fratzl and I. Zlotnikov, *Nat. Mater.*, 2014, **13**, 1102–1107.
49 V. Schoeppler, L. Gránásy, E. Reich, N. Poulsen, R. de Kloe, P. Cook, A. Rack, T. Pusztai and I. Zlotnikov, *Adv. Mater.*, 2018, **30**, 1803855.
50 V. Schoeppler, D. Stier, R. J. Best, C. Song, J. Turner, B. H. Savitzky, C. Ophus, M. A. Marcus, S. Zhao, K. Bustillo and I. Zlotnikov, *Adv. Mater.*, 2021, 2101358.
51 E. Weber and B. Pokroy, *CrystEngComm*, 2015, **17**, 5873–5883.
52 J. Villanova, S. Kozachkevich, P. Zaslansky, L. Kundanati, A. A. Bracha, I. Polishchuk, L. Bloch, D. Levy, A. Katsman, C. Giacobbe, Y. Etinger-Geller, P. Gilbert, B. Pokroy, A. J. Giuffre, M. A. Marcus, N. M. Pugno, Y. Kauffmann, G. Hendler, M. Burghammer and C.-Y. Sun, *Science*, 2017, **358**, 1294–1298.
53 F. Mastropietro, P. Godard, M. Burghammer, C. Chevallard, J. Daillant, J. Duboisset, M. Allain, P. Guenoun, J. Nouet and V. Chamard, *Nat. Mater.*, 2017, **16**, 946–952.
54 S. E. Wolf, N. Loges, B. Mathiasch, M. Panthöfer, I. Mey, A. Janshoff and W. Tremel, *Angew. Chem.*, 2007, **119**, 5716–5721.
55 A. Berman, J. Hanson, L. Leiserowitz, T. F. Koetzle, S. Weiner and L. Addadi, *Science*, 1993, **259**, 776–779.
56 Z. Deng, H. Chen, T. Yang, Z. Jia, J. C. Weaver, P. D. Shevchenko, F. De Carlo, R. Mirzaeifar and L. Li, *Nat. Commun.*, 2020, **11**, 5678.
57 P. Gilbert, A. Young and S. N. Coppersmith, *Proc. Natl. Acad. Sci. U. S. A.*, 2011, **108**, 11350–11355.
58 Y. Dauphin, *J. Biol. Chem.*, 2003, **278**, 15168–15177.
59 T. Okumura, M. Suzuki, H. Nagasawa and T. Kogure, *Cryst. Growth Des.*, 2012, **12**, 224–230.
60 T. Okumura, M. Suzuki, H. Nagasawa and T. Kogure, *Micron*, 2010, **41**, 821–826.
61 A. G. Checa, J. T. Bonarski, M. G. Willinger, M. Faryna, K. Berent, B. Kania, A. González-Segura, C. M. Pina, J. Pospiech and A. Morawiec, *J. R. Soc., Interface*, 2013, **10**, 20130425.
62 A. G. Checa, F. J. Esteban-Delgado, J. Ramírez-Rico and A. B. Rodríguez-Navarro, *J. Struct. Biol.*, 2009, **167**, 261–270.
63 R. Hovden, S. E. Wolf, M. E. Holtz, F. Marin, D. A. Muller and L. A. Estroff, *Nat. Commun.*, 2015, **6**, 10097.
64 P. Gilbert, R. A. Metzler, D. Zhou, A. Scholl, A. Doran, A. Young, M. Kunz, N. Tamura and S. N. Coppersmith, *J. Am. Chem. Soc.*, 2008, **130**, 17519–17527.
65 I. C. Olson, R. Metzler, N. Tamura, M. Kunz, C. E. Killian and P. Gilbert, *J. Struct. Biol.*, 2013, **183**, 180–190.
66 A. G. Shtukenberg, Y. O. Punin, E. Gunn and B. Kahr, *Chem. Rev.*, 2012, **112**, 1805–1838.
67 Y.-Y. Kim, J. D. Carloni, B. Demarchi, D. Sparks, D. G. Reid, M. E. Kunitake, C. C. Tang, M. J. Duer, C. L. Freeman, B. Pokroy, K. Penkman, J. H. Harding, L. A. Estroff, S. P. Baker and F. C. Meldrum, *Nat. Mater.*, 2016, **15**, 903–910.
68 D. Athanasiadou, W. Jiang, D. Goldbaum, A. Saleem, K. Basu, M. S. Pacella, C. F. Böhm, R. R. Chromik, M. T. Hincke, A. B. Rodríguez-Navarro, H. Vali, S. E. Wolf, J. J. Gray, K. H. Bui and M. D. McKee, *Sci. Adv.*, 2018, **4**, 1–14.
69 Y. Dauphin, E. Zolotoyabko, A. Berner, E. Lakin, C. Rollion-Bard, J. P. Cuif and P. Fratzl, *J. Struct. Biol.*, 2019, **205**, 121–132.
70 D. P. Grigoriev, *Otogeny of Minerals*, Israel Programme for Scientific Translations, Jerusalem, 1965.
71 J. Harris, I. Mey, M. Hajir, M. Mondeshki and S. E. Wolf, *CrystEngComm*, 2015, **17**, 6831–6837.
72 H.-J. Bunge, *Texture Analysis in Materials Science*, Butterworth-Heinemann, Oxford, UK, 2013.
73 D. Mainprice, R. Hielscher and H. Schaeben, *Geol. Soc. Spec. Publ.*, 2011, **360**, 175–192.
74 C. C. Chen, C. C. Lin, L. G. Liu, S. V. Sinogeikin and J. D. Bass, *Am. Mineral.*, 2001, **86**, 1525–1529.
75 M. Strąg, Ł. Maj, M. Bieda, P. Petrzak, A. Jarzębska, J. Gluch, E. Topal, K. Kutukova, A. Clausner, W. Heyn, K. Berent, K. Nalepka, E. Zschech, A. G. Checa and K. Sztwiertnia, *Nanomaterials*, 2020, **10**, 634.
76 S. Amini and A. Miserez, *Acta Biomater.*, 2013, **9**, 7895–7907.
77 G. M. Pharr, *Mater. Sci. Eng., A*, 1998, **253**, 151–159.
78 B. Merle, W. H. Higgins and G. M. Pharr, *J. Mater. Res.*, 2020, **35**, 343–352.
79 K. E. Johanns, J. H. Lee, Y. F. Gao and G. M. Pharr, *Modell. Simul. Mater. Sci. Eng.*, 2014, **22**, 015011.
80 A. E. Giannakopoulos and S. Suresh, *Int. J. Solids Struct.*, 1997, **34**, 2357–2392.
81 A. E. Giannakopoulos and S. Suresh, *Int. J. Solids Struct.*, 1997, **34**, 2393–2428.
82 H. Yao and H. Gao, *J. Comput. Theor. Nanosci.*, 2010, **7**, 1299–1305.
83 D. C. Pender, N. P. Padture, A. E. Giannakopoulos and S. Suresh, *Acta Mater.*, 2001, **49**, 3255–3262.
84 D. C. Pender, S. C. Thompson, N. P. Padture, A. E. Giannakopoulos and S. Suresh, *Acta Mater.*, 2001, **49**, 3263–3268.
85 S. Suresh, *Science*, 2001, **292**, 2447–2451.
86 J.-P. Cuif, M. Burghammer, V. Chamard, Y. Dauphin, P. Godard, G. Moullac, G. Nehrke and A. Perez-Huerta, *Minerals*, 2014, **4**, 815–834.
87 S. S. Chiang, D. B. Marshall and A. G. Evans, *J. Appl. Phys.*, 1982, **53**, 298–311.
88 X. Chen, J. W. Hutchinson and A. G. Evans, *J. Am. Ceram. Soc.*, 2005, **88**, 1233–1238.
89 S. E. Wolf, C. F. Böhm, J. Harris, B. Demmert, D. E. Jacob, M. Mondeshki, E. E. Ruiz-Agudo and C. Rodriguez-Navarro, *J. Struct. Biol.*, 2016, **196**, 260–287.
90 J. Gim, N. Schnitzer, L. M. Otter, Y. Cui, S. Motreuil, F. Marin, S. E. Wolf, D. E. Jacob, A. Misra and R. Hovden, *Nat. Commun.*, 2019, **10**, 4822.
91 M. Rousseau, E. Lopez, P. Stempflé, M. Brendlé, L. Franke, A. Guette, R. Naslain and X. Bourrat, *Biomaterials*, 2005, **26**, 6254–6262.

92 C. Rodríguez-Navarro, E. Ruiz-Agudo, J. Harris and S. E. Wolf, *J. Struct. Biol.*, 2016, **196**, 260–287.
93 D. Ectors, F. Goetz-Neunhoeffer and J. Neubauer, *J. Appl. Crystallogr.*, 2015, **48**, 189–194.
94 G. Porod, *Kolloid-Z.*, 1951, **124**, 108–122.
95 G. Zhang and J. Xu, *J. Struct. Biol.*, 2013, **182**, 36–43.
96 G. Beaucage, *J. Appl. Crystallogr.*, 1995, **28**, 717–728.
97 A. Baronnet, J.-P. Cuif, Y. Dauphin, B. Farre and J. Nouet, *Mineral. Mag.*, 2008, **72**, 617–626.
98 W. Huang, D. Restrepo, J. Jung, F. Y. Su, Z. Liu, R. O. Ritchie, J. McKittrick, P. Zavattieri and D. Kisailus, *Adv. Mater.*, 2019, **31**, 1901561.
99 H. Loh, T. Divoux, B. Gludovatz, P. U. P. A. Gilbert, R. O. Ritchie, F. Ulm and A. Masic, *Commun. Mater.*, 2020, **1**, 77.
100 R. Roer and R. Dillaman, *Am. Zool.*, 1984, **24**, 893–909.
101 D. Chateigner, C. Hedegaard and H. Wenk, in *11th International Conference on Textures of Materials*, ed. Z. Liang, L. Zuo and Y. Chu, International Academic Publishers, 1996, vol. 2, pp. 1221–1226.
102 A. G. Checa and A. B. Rodríguez-Navarro, *Proc. R. Soc. London, Ser. B*, 2001, **268**, 771–778.
103 W. Wagermaier, H. S. Gupta, A. Gourrier, O. Paris, P. Roschger, M. Burghammer, C. Riekel and P. Fratzl, *J. Appl. Crystallogr.*, 2007, **40**, 115–120.